Inorganic Chemistry

Article

pubs.acs.org/IC

Femtosecond Study of Dimolybdenum Paddlewheel Compounds with Amide/Thioamide Ligands: Symmetry, Electronic Structure, and Charge Distribution in the ^{1}MLCT S_1 State

Changcheng Jiang,* Philip J. Young,† Samantha Brown-Xu,‡ Judith C. Gallucci, and Malcolm H. Chisholm

Department of Chemistry and Biochemistry, The Ohio State University, 100 West 18th Avenue, Columbus, Ohio 43210, United States

Supporting Information

ABSTRACT: Four photophysically interesting dimolybdenum paddlewheel compounds are synthesized and characterized: **I** and **II** contain amide ligand (*N*,3-diphenyl-2-propynamide), and **III** and **IV** contain thioamide ligand (*N*,3-diphenyl-2-propynethioamide). **I** and **III** are *trans*-$Mo_2L_2(O_2C\text{-}T^iPB)_2$-type compounds, and **II** and **IV** are Mo_2L_4-type compounds, where $O_2C\text{-}T^iPB$ is 2,4,6-triisopropylbenzoate. **I**–**IV** display strong light absorption due to metal to ligand charge transfer (MLCT) transitions from molybdenum to the amide/thioamide ligands. Charge transfer dynamics in the MLCT excited states of **I**–**IV** have been examined using femtosecond transient absorption (fs-TA) spectroscopy and femtosecond time-resolved infrared (fs-TRIR) spectroscopy. The asymmetric amide/thioamide ligands show two forms of regioarrangements in the paddlewheel compounds. Analyses of the ν(C≡C) bands in the fs-TRIR spectra of **I** and **II** show similar electron density distribution over ligands in their ^{1}MLCT S_1 states where only two amide ligands are involved and the transferred electron is mainly localized on one of them. The fs-TRIR spectra of **III** and **IV**, however, show different charge distribution patterns where the transferred electron is fully delocalized over two thioamide ligands in **III** and partially delocalized in **IV**. Fast interligand electron transfer (ILET) was recognized as the explanation for the various charge distribution patterns, and ILET was shown to be influenced by both the ligands and the ligand arrangements.

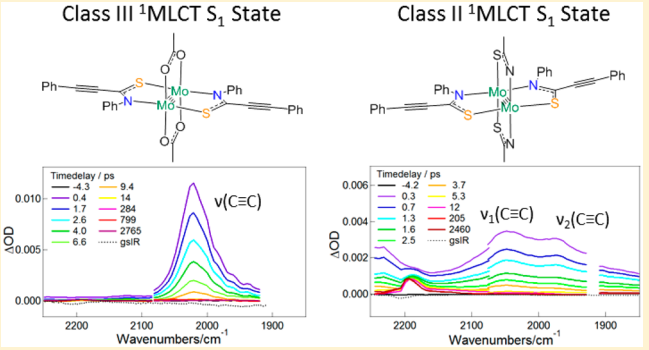

INTRODUCTION

Transition metal (TM) compounds showing strong light absorption due to MLCT transitions have found wide applications as photosensitizers, photocatalysts, and luminescent materials.[1−4] Upon absorption of a photon at the MLCT bands, an electron moves from a metal-based orbital into a ligand-based orbital which leaves the compounds in charge-separated MLCT states. With multiple acceptor ligands, the transferred electron in the MLCT states of TM compounds can have various distribution patterns: the electron could be localized on one ligand or delocalized over two or more ligands.[5−9] Such differences would strongly influence the photophysical and photochemical properties of TM compounds, yet charge distributions in MLCT states have not been routinely addressed due to quick relaxation of the excited states. Similar localization−delocalization problems also have been observed in other systems such as the excited states of branched organic compounds and also the ground states of certain radicals.[10−13]

Mo_2 and W_2 quadruply bonded compounds provide convenient models for the study of charge dynamics in their MLCT states (especially the lowest singlet excited states, i.e., ^{1}MLCT S_1 states) due to their simple structure and high symmetry.[14] Unlike many mononuclear complexes, Mo_2 and W_2 compounds have ^{1}MLCT S_1 states that are sufficiently long lived to be carefully examined by femtosecond transient absorption (fs-TA) and femtosecond time-resolved infrared (fs-TRIR) experiments.[15−17] A fair number of Mo_2 and W_2 compounds with carboxylate ligands have been studied, typically in the form of *trans*-$M_2L_2L'_2$ and M_2L_4 (with two and four acceptor ligands, respectively, as shown in Figure 1). A bulky carboxylate ligand with twisted accepting groups, 2,4,6-triisopropylbenzoate ($O_2C\text{-}T^iPB$), was frequently used as an auxiliary ligand in the *trans*-$M_2L_2L'_2$ compounds for synthetic convenience and also because the ligand only allows high-energy MLCT transitions.[18]

With IR reporter groups such as C≡C and C≡N bonds, additional electron density on the ligands in the excited states of *trans*-$M_2L_2(O_2C\text{-}T^iPB)_2$ and M_2L_4 compounds can be

Received: October 19, 2016

DOI: 10.1021/acs.inorgchem.6b02517
Inorg. Chem. XXXX, XXX, XXX−XXX

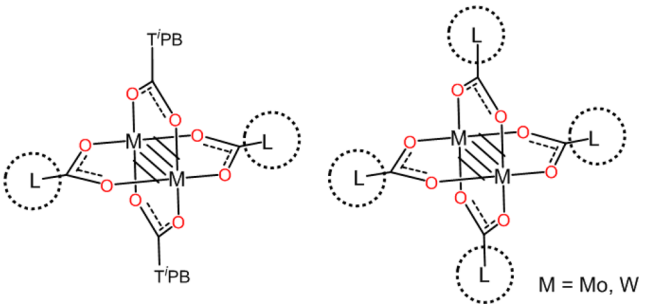

Figure 1. General structure of *trans*-$M_2L_2(O_2C\text{-}T^iPB)_2$ and M_2L_4 paddlewheel compounds with carboxylate ligands where M is Mo or W.

directly observed through the shift of $\nu(C{\equiv}C)$ and $\nu(C{\equiv}N)$ bands in fs-TRIR spectra.[16,19,20] Both localized and delocalized ^{1}MLCT S_1 states were found in these compounds with different acceptor ligands.[14,21] The transition from localized charge distribution to delocalized charge distribution appears to be connected with interligand electron transfer (ILET) on the IR time scale ($\sim10^{-12}$ s) where "fast" ILET would present as if the electron were delocalized while "slow" ILET would present as if the electron were localized.[5,22] Such ligand-based electron transfer process is supported by the presence of mixed-valence (MV) states in Mo_2 and W_2 paddlewheel radical anions.[23] The bridging units, which include the dimetal center and ligand donor atoms, were determined to play an important role in the ILET process.[21] Also, the fs-TRIR spectra of *trans*-$M_2L_2(O_2C\text{-}T^iPB)_2$ and M_2L_4 compounds with the same acceptor ligands were generally found to be similar.[16,20] Such observations suggest that only trans ligands are involved in the fast ILET process.

Previously, in the amidinate−carboxylate compound *trans*-$Mo_2[(^iPrN)_2CC{\equiv}CPh]_2(O_2CMe)_2$, we discovered that the charge distribution on the amidinate ligands in the ^{1}MLCT S_1 state is a borderline case,[16] i.e., the majority of the electron density is localized on one of the amidinate ligands but some electron density is also present on the other ligand. Due to the similarities between this type of excited-state species and a class II MV compound, we classified it as a class II ^{1}MLCT S_1 state. Follow-up studies on compounds *trans*-$Mo_2[(PhN)_2CC{\equiv}CPh]_2(O_2C\text{-}T^iPB)_2$ and $Mo_2[(PhN)_2CC{\equiv}CPh]_4$ have shown that the charge distribution can be tuned, and the total localization case was found in the latter compound.[24] These observations prompted us to investigate compounds with similar ligand sets.

To understand the role of the bridging units in interligand electron transfer, we set to change the electronic structure of the Mo_2 compounds. Here, we prepared Mo_2 paddlewheel compounds **I**−**IV** with amide and thioamide ligands where one of the nitrogen atoms in the amidinate ligands is substituted by an oxygen or a sulfur atom. The amide and thioamide ligands are shown in Figure 2 together with $O_2C\text{-}T^iPB$. The 2p orbitals of oxygen are lower in energy in comparison to nitrogen, and sulfur instead has more diffuse 3p orbitals. The substitution created significant electronic structure changes. Since amide and thioamide ligands are asymmetric compared to carboxylate and amidinate ligands, different regioarrangements also appeared in these paddlewheel compounds.[25]

The structures of the *trans*-$M_2L_2L'_2$ compounds **I** and **III** were studied using single-crystal X-ray crystallography; together with the previously reported structures of M_2L_4 homoleptic

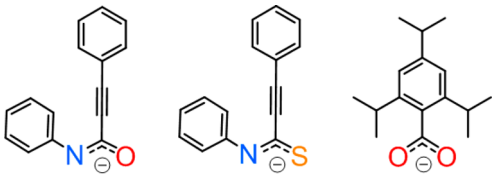

Figure 2. Structure of *N*,3-diphenyl-2-propynamide, *N*,3-diphenyl-2-propynethioamide, and 2,4,6-triisopropylbenzoate ligands.

compounds **II** and **IV**,[26] it was found that the amide/thioamide ligands are centrosymmetrically disposed to each other in **I**−**III** while adopting a mirror-symmetric arrangement in **IV**. The photophysical properties of **I**−**IV** were thoroughly examined using steady-state absorption, emission, and time-resolved spectroscopic methods. The excited-state charge distribution patterns were found to be similar in **I** and **II** but distinctively different in **III** and **IV**. Electronic transitions of **I**−**IV** were investigated with density functional theory (DFT) and time-dependent density functional theory (TD-DFT) methods. Correlations between electronic structures and excited-state charge dynamics are discussed.

EXPERIMENTAL SECTION

General Procedures. Compounds **I**−**IV** are air and moisture sensitive, especially so in solution. Syntheses and handling of all four compounds were conducted using standard Schlenk line and glovebox techniques. All solvents used were thoroughly dried and degassed following standard protocols.[27]

Syntheses. The preparative methods for compounds **I**−**IV** are displayed in Scheme 1. Two dimolybdenum carboxylates, $Mo_2(O_2C\text{-}T^iPB)_4$ and $Mo_2(OAc)_4$, were used as starting materials, and they were synthesized conveniently following literature methods.[18,25] **I** and **III** were prepared by reacting $Mo_2(O_2C\text{-}T^iPB)_4$ with two equivalents of ligand (lithium *N*,3-diphenyl-2-propynamide and lithium *N*,3-diphenyl-2-propynethioamide, respectively); **II** and **IV** were prepared by reacting $Mo_2(OAc)_4$ with four equivalents of ligand.[26] Compounds **I**−**IV** were purified through solution processes, and the purity of each compound was confirmed by ^{1}H NMR and MALDI-TOF mass spectra. Details of ligand and compound syntheses and NMR and MALDI-TOF mass spectra for **I**−**IV** are included in the Supporting Information.

Scheme 1. Preparation of I−IV

Eq 1. $Mo_2(O_2C\text{-}T^iPB)_4 + 2Li^+(L)^-$ $\xrightarrow[1\ day]{THF}$ $Mo_2(L)_2(O_2C\text{-}T^iPB)_2 + 2Li^+(O_2C\text{-}T^iPB)^-$ **(I, III)**

Eq 2. $Mo_2(OAc)_4 + 4Li^+(L)^-$ $\xrightarrow[1\ day]{THF}$ $Mo_2(L)_4 + 4Li^+(OAc)^-$ **(II, IV)**

X-ray Crystallography. Crystals of **I** and **III** suitable for single-crystal X-ray diffraction were grown by diffusion of hexanes into concentrated THF solutions of **I** and **III** containing a small amount of DMSO. Diffraction data were collected on a Nonius Kappa Apex II CCD diffractometer with Mo Kα radiation. All work was done at 150 K using an Oxford Cryosystems Cryostream Cooler. X-ray crystallographic data in CIF format can be found in the Supporting Information. Crystal data and selected bond lengths are also included as Tables S1 and S2 in the Supporting Information. The structures of **II** and **IV** have been reported previously.[26]

Absorption and Emission Spectra. Absorption spectra of **I**−**IV** were record on a PerkinElmer Lambda 900 spectrometer. Data were collected from 250 to 800 nm in THF solution using a 1 cm × 1 cm quartz cell. The cell is equipped with a Kontes stopcock. Molar extinction coefficients (ε) of **I**−**IV** were calculated from absorbance

DOI: 10.1021/acs.inorgchem.6b02517
Inorg. Chem. XXXX, XXX, XXX−XXX

values at four different concentrations. Emission spectra of **I**–**IV** were obtained with the Jabin Yvon Fluorolog 3 fluorometer equipped with a Synapse CCD detector. Data were collected from 500 to 1100 nm in 2-methyl tetrahydrofuran (2-MeTHF) solution in a J. Young tube at both room temperature and 77 K with a customized Dewar cuvette.

Electronic Structure Computation. Structure optimizations of **I**–**IV** were performed using density functional theory (DFT) methods with the B3LYP functional in the Gaussian 09 suite.[28] The 6-31G(d) basis set was used for all nonmetal elements; the SDD energy-consistent pseudopotentials and the SDD energy-consistent basis set were used for Mo atoms.[29] Atomic coordinates from crystal structures were used as the initial input. Time-dependent density functional theory (TD-DFT) calculations were carried out for **I**–**IV** to study the electronic transitions.

DFT calculations were also performed on **I**–**IV** in their triplet states and **I**–**IV** bearing one negative charge ("molecular anions", mimics of the MLCT singlet states) to aid the interpretation of fs-TRIR spectra. To cut computational costs in these open-shell calculations, phenyl groups on the nitrogen atoms and aryl groups in the O_2C-T^{i}PB ligands were replaced with hydrogen atoms, and these results will be referred to with a prime notation (for example, ^{3}**I′** represents the calculated triplet state of **I**, and **I′**$^-$ represents the calculated molecular anion of **I**). All vibrational frequency results were scaled by a factor of 0.961 as suggested.[30]

Femtosecond and Nanosecond Time-Resolved Spectroscopy. Femtosecond transient absorption spectroscopy (fs-TA) and femtosecond time-resolved infrared spectroscopy (fs-TRIR) experiments were performed with a Ti:sapphire laser system (1 kHz, fwhm ≈ 300 fs) as described previously.[31,32] In the fs-TA experiments, sample solutions were prepared in THF with an absorbance of ∼0.4 at the maximum of the MLCT band and kept in a 1.0 mm quartz cuvette with a Kontes stopcock. In the fs-TRIR experiments, the sample solutions were prepared in THF as well with an absorbance of ∼1 at the maximum of the MLCT band and were sealed in a PerkinElmer semidemountable cell with a 0.1 mm Teflon spacer between two 4 mm CaF_2 windows. The excitation wavelength was set at 515 nm for **I**–**III** and at 568 nm for **IV** in both fs-TA and fs-TRIR experiments, and the excitation power was set at 1–2 μJ at the samples. fs-TA spectra from 300 to 700 nm and fs-TRIR spectra from 1350 to 2250 cm^{-1} were collected for **I**–**IV**.

Nanosecond transient absorption (ns-TA) spectra were performed on a home-built instrument equipped with a Spectra-Physics GCR-150 Nd:YAG laser source (fwhm ≈ 10 ns) and a Hamamatsu R928 photomultiplier tube. Transient signals were processed with a Tektronics 400 MHz oscilloscope. The excitation wavelengths were set at 532 nm for **I**–**IV**, and the excitation power was set at ∼100 mW at the samples. Sample solutions were prepared in THF with an absorbance of ∼0.3 at the maximum of the MLCT band and kept in a 1 cm × 1 cm quartz cuvette with a Kontes stopcock. ns-TA spectra from 380 to 760 nm were collected for **I**–**IV**.

All time-resolved spectra were plotted in Igor Pro 6.0. Kinetic traces were fitted with a global fitting package with a sum of exponentials, $S(t) = \sum_i A_i \exp(-1/\tau_i) + C$, where A_i is the amplitude, τ_i is the lifetime, and C is an offset.

RESULTS AND DISCUSSION

X-ray Crystal Structure. With the asymmetric bridging ligands, the core structures of **I**, **II**, **III**, and **IV** show reduced symmetry from the ideal D_{2h} and D_{4h} symmetry for *trans*-$M_2L_2L'_2$ and M_2L_4 compounds.

The crystal structures of **I** and **II** are shown in Figure 3. The core structures of **I** and **II** have the same C_{2h} pseudo symmetry. The two amide ligands in **I** are centrosymmetrically disposed to each other, and the same arrangement is found for each set of the *trans*-amide ligands in **II**. Overall, **II** adopts the so-called "*cis*-2,2" structure.[26]

The crystal structures of **III** and **IV** are shown in Figure 4. The core structures of **III** and **IV** have the C_{2h} and D_{2d} pseudo symmetry, respectively. The two thioamide ligands in **III** are centrosymmetrically disposed to each other, similar to **I**. Each set of the *trans*-thioamide ligands in **IV** instead has a mirror-reflection relationship. Overall **IV** adopts the "*trans*-2,2" structure.[26]

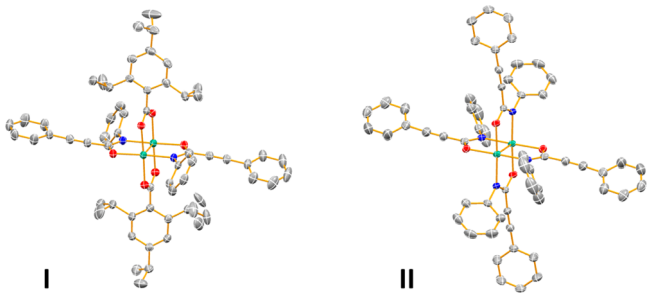

Figure 3. Crystal structures of **I** and **II**. Green = molybdenum, blue = nitrogen, red = oxygen, and gray = carbon. Hydrogen atoms and solvent molecules were obscured for clarity. (Plot of **II** was adapted from ref 26 with permission of The Royal Society of Chemistry.)

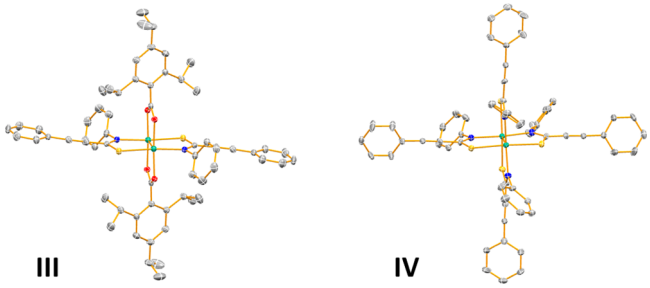

Figure 4. Crystal structures of **III** and **IV**. Green = molybdenum, blue = nitrogen, red = oxygen, gray = carbon, and yellow = sulfur. Hydrogen atoms and solvent molecules were obscured for clarity. (Plot of **IV** was adapted from ref 26 with permission of The Royal Society of Chemistry.)

As shown by Berry and co-workers, the configuration of Mo_2 amide/thioamide compounds changes with different amide and thioamide ligands.[33] However, no isomers were isolated in the synthetic process, and no isomers are expected to exist in solution as a result of the nonlabile nature of the Mo–N bonds.[26,33]

In all four compounds, extended conjugation is expected along the *trans*-L–Mo_2–L chains. The metal atoms and the N–C–X bridging ligands are almost coplanar with the —C≡C—Ph moieties. This is more pronounced in **I** and **III** than in **II** and **IV**. The phenyl groups on the nitrogen atoms are twisted by ∼60° from the N–C–X planes in all four compounds, effectively removing them from contributing to the conjugation. This is also true for the aryl groups in the O_2C-T^{i}PB ligands, which are twisted by 80–90° from the CO_2 planes.

Compounds **I**–**IV** show Mo–Mo bond lengths of ∼2.10 Å, which is typical of Mo_2 quadruple bonds.[25] Average Mo–N bond length in all compounds is ∼2.13 Å; average Mo–O bond length is ∼2.10 Å (between Mo_2 and amide ligands), and average Mo–S bond length is ∼2.46 Å. Due to the longer Mo–S bonds, the —C≡C—Ph groups in **III** and **IV** deviate slightly from the perpendicular position with respect to the Mo–Mo quadruple bond. Distance between the centers of C≡C bonds on trans amide/thioamide ligands is ∼9.6 Å in **I** and **II** and ∼10.0 Å in **III** and **IV**.

DOI: 10.1021/acs.inorgchem.6b02517
Inorg. Chem. XXXX, XXX, XXX–XXX

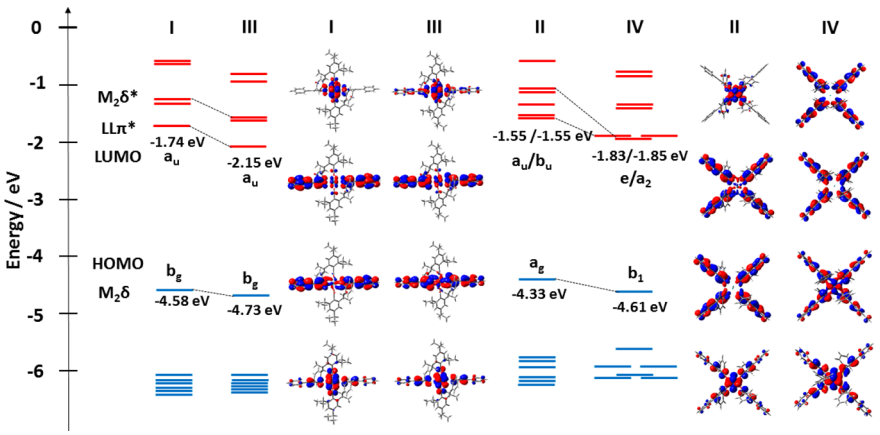

Figure 5. MO energy diagrams and selected orbital surfaces of **I**–**IV**. MO surfaces were plotted with Gaussian 5.08, and idealized symmetries were assigned. From top to bottom, surface plots of LUMO+2 (a_u, δ^*), LUMO+1 (b_g, LLπ^*), LUMO (a_u, LLπ^*), and HOMO (b_g, δ) are shown for **I** and **III**; LUMO+4 (a_u, δ^*), LUMO+1 (a_u, LLπ^*), LUMO (b_u, LLπ^*), and HOMO (b_g, δ) are shown for **II**; LUMO+2 (e, LLπ^*), LUMO+1 (e, LLπ^*), LUMO (a_2, LLπ^*+δ^*), and HOMO (b, δ) are shown for **IV**.

Electronic Structure and Electronic Transitions. Electronic structures of **I**–**IV** were investigated using DFT methods. Molecular orbital (MO) energy levels, symmetry, and frontier orbital surface plots are presented in Figure 5. Natural bonding orbital (NBO) analyses were carried out to study the orbital compositions.[34,35] The contributions of metal orbitals to the frontier orbitals of **I**–**IV** are summarized in Table 1. The increase in metal–ligand orbital mixing is significant with the asymmetric ligands and with the introduction of sulfur atoms.

Table 1. Mo_2 Contribution (%) to Frontier Molecular Orbitals Calculated from NBO Analysis

	HOMO	LUMO	LUMO+1	LUMO+2	LUMO+3	LUMO+4
I	65.4	3.4	7.2	76.2		
II	58.6	0.7	3.3	0.1	74.4	10.1
III	60.0	9.9	7.6	69.2		
IV	51.2	33.2	1.2	1.2	39.2	13.0

Electronic structures of *trans*-$Mo_2L_2(O_2C\text{-}T^iPB)_2$ and Mo_2L_4 are best described by interactions between the ligand π^* orbitals (the combination of which will be referred to as LLπ^* orbitals) and Mo–Mo quadruple bond orbitals.[23] The highest occupied molecular orbital (HOMO) in *trans*-$Mo_2L_2(O_2C\text{-}T^iPB)_2$ and Mo_2L_4 compounds is typically composed of the $Mo_2\delta$ orbital, and the lowest unoccupied molecular orbital (LUMO) is usually composed of one of the LLπ^* orbitals.

In **I** and **III**, the π^* orbitals of the two amide/thioamide ligands combine and transform as a_u and b_g symmetry in the C_{2h} point group. The $Mo_2\delta$ orbital transforms as b_g symmetry, and the $Mo_2\delta^*$ orbital transforms as a_u symmetry. The b_g LLπ^* orbital interacts with the $Mo_2\delta$ orbital and is raised in energy relative to the a_u LLπ^* orbital. The resulting HOMO is a $Mo_2\delta$-based orbital with b_g LLπ^* contribution. The resulting LUMO is essentially the a_u LLπ^* orbital with some $Mo_2\delta^*$ orbital character.

The increase of metal orbital character in the LUMO of **I** and **III** is significant with the symmetry reduction.[20,24] Also, due to the lower π^* orbital energy of the thioamide ligand and the more diffuse p orbitals of the sulfur atom, **III** shows a lower energy HOMO, a lower energy LUMO, and stronger metal–ligand orbital mixing in comparison to **I**. The NBO analysis shows that the ligand orbitals contribute ~40% to the HOMO of **III** compared to ~35% to the HOMO of **I**. In addition, metal orbitals contribute 9.9% to the LUMO of **III** compared to 3.4% to the LUMO of **I**.

In **II** and **IV**, the four ligand π^* orbitals combine and transform into four different LLπ^* combinations, namely, the b_u, a_u, b_g, and a_g LLπ^* orbitals in **II** (C_{2h} point group) and a_2, e, and b_1 LLπ^* orbitals in **IV** (D_{2d} point group). The arrangement and composition of LLπ^* orbitals in **II** and **IV** appear to be very different from each other due to the ligand arrangements. In **II**, the a_u and b_u LLπ^* orbitals become the LUMO and LUMO+1, and their energy levels are very close. Transitions from HOMO to LUMO and LUMO+1 are both fully allowed.

Table 2. Electronic Transitions in Compounds I–IV Predicted by TD-DFT[a]

		origin	λ (nm)	f
I	$S_0 \rightarrow S_1$	HOMO → 0.54 LUMO, 0.42 LUMO+2 (δ^*)	512	0.360
	$S_0 \rightarrow S_2$	HOMO → 0.53 LUMO+2 (δ^*), 0.44 LUMO	492	0.367
	$S_0 \rightarrow S_{10}$	HOMO → 0.57 LUMO+6, 0.41 LUMO+4	352	0.285
II	$S_0 \rightarrow S_1$	HOMO → 0.68 LUMO+1, 0.15 LUMO+4 (δ^*)	516	0.593
	$S_0 \rightarrow S_2$	HOMO → 0.70 LUMO	512	0.749
III	$S_0 \rightarrow S_1$	HOMO → 0.66 LUMO, 0.22 LUMO+2 (δ^*)	570	0.421
	$S_0 \rightarrow S_2$	HOMO → 0.64 LUMO+2 (δ^*), 0.23 LUMO	489	0.338
IV	$S_0 \rightarrow S_1$	HOMO → 0.67 LUMO (δ^*), 0.16 LUMO+4	560	0.015
	$S_0 \rightarrow S_2$	HOMO → 0.68 LUMO+1, 0.13 LUMO+2	521	0.556

[a]Notes: λ is the transition wavelength, and f is the oscillator strength.

DOI: 10.1021/acs.inorgchem.6b02517
Inorg. Chem. XXXX, XXX, XXX–XXX

In **IV**, the a_2 LLπ* orbital with strong $Mo_2\delta$* orbital character turns out to be the LUMO instead of the e LLπ* orbitals normally found in Mo_2 homoleptic carboxylate compounds.[14] The $Mo_2\delta$* orbital contributes greatly to the LUMO of **IV** (33%). The HOMO → LUMO transition in **IV** is symmetry allowed with the absence of an inversion center.

TD-DFT calculations were also carried out for compounds **I**–**IV** to study the electronic transitions. The results are summarized in Table 2.

As expected, the HOMO → LUMO transitions, which are MLCT in nature, are the dominant transitions in all of the compounds except **IV**. In **IV**, the oscillator strength of the HOMO → LUMO transition is weak while the HOMO → LUMO+1 transition appears to be the dominant transition. Since the LUMO+1/LUMO+2 of **IV** are similar to the e-type LUMO/LUMO+1 normally found for homoleptic carboxylate compounds, the HOMO → LUMO+1 transition in **IV** is still a typical MLCT transition. It is worth noting that in the MLCT excited states of **II** and **IV**, Jahn–Teller distortions are expected to appear when the electron is transferred into the close-to-degenerate LLπ* orbitals, as described previously.[20,24]

The calculations also predicted that there is a specific and intense metal-based $\delta \rightarrow \delta^*$ transition in **I** and **III** at slightly higher energies of the MLCT transition. The mixing of MLCT transitions in the metal-based $\delta \rightarrow \delta^*$ transition is unexpectedly strong. Generally, the $\delta \rightarrow \delta^*$ absorption bands were weak in the previously studied carboxylate and amidinate compounds.[20,24,36]

UV–vis Absorption and Emission. The absorption spectra of **I**–**IV** recorded in THF solution at room temperature are shown in Figure 6. Generally, the compounds show strong ligand-based absorption bands in the UV region and MLCT absorption bands the visible region.

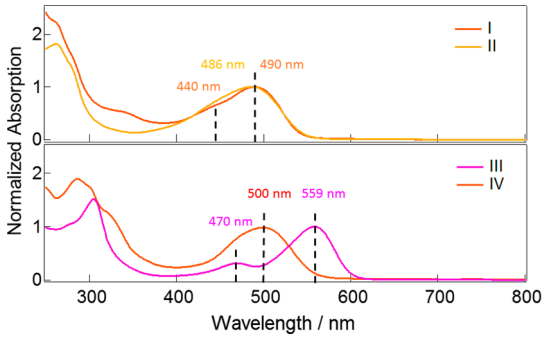

Figure 6. Normalized UV–vis absorption spectra of **I**–**IV**. Spectra were recorded in THF solution at room temperature.

Compounds **I** and **II**, with amide ligands, show MLCT absorption bands at 490 and 486 nm, respectively. The molar extinction coefficient ε was determined to be 18 600 M^{-1} cm^{-1} at the MLCT band of **I** and 31 600 M^{-1} cm^{-1} of **II**. These MLCT bands have steeper slopes on the low-energy side. There is a shoulder at the MLCT band of **I** appearing at ~440 nm, which was assigned to the $\delta \rightarrow \delta^*$ transition. The absorption band at ~350 nm in **I** was assigned to the higher energy MLCT transition to the O_2C-T^{i}PB ligands.

Compound **III** shows two absorption bands in the visible region with one at 470 nm (ε = 5600 M^{-1} cm^{-1}) and the other at 559 nm (ε = 19 700 M^{-1} cm^{-1}). The 559 nm band was assigned to the MLCT transition and the 470 nm band to the $\delta \rightarrow \delta^*$ transition. The splitting between the two transitions in **III** is larger than that of **I**, agreeing with TD-DFT calculations. Also in **III**, the expected MLCT transition to O_2C-T^{i}PB ligand is obscured in the ligand-based transitions. In **IV**, the strongest absorption band in the visible region appears at 500 nm (ε = 42 300 M^{-1} cm^{-1}). The predicted low-intensity HOMO → LUMO transition at 560 nm indeed cannot be identified. The transitions in **III** and **IV** are generally stronger than those in **I** and **II**, as shown by the molar extinction coefficients.

Emission spectra of **I**–**IV** from the visible to the near-infrared region were taken in 2-MeTHF solution at room temperature and at 77 K. The spectra are shown in Figure 7,

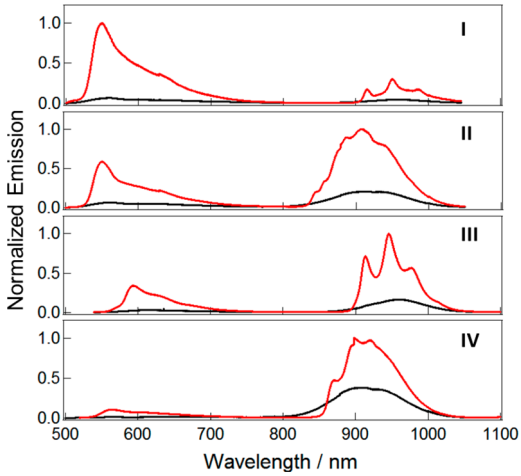

Figure 7. Normalized emission spectra of **I**–**IV**. Emission spectra at room temperature are shown in black, and emission at 77 K are shown in red. Spectra were recorded in 2-MeTHF.

and the peak wavelengths are summarized in Table 3. Emissions from both singlet states (fluorescence) and from triplet states (phosphorescence) were observed for all four compounds.

Table 3. Emission Peaks of I–IV Recorded in 2-MeTHF at Room Temperature (RT) and at 77 K

	fluorescence (nm)		phosphorescence (nm)	
	RT	77 K	RT	77 K
I	562	550	952	951
II	560	551	909	908
III	604	593	969	946
IV	565	563	912	898

The fluorescence of **I**–**IV** was determined to be from the ^{1}MLCT states and the phosphorescence from the $^3\delta\delta$* states based on their energy, band shape, and vibronic progressions at low temperature.[14] Typically, the fluorescence maxima were observed 1000–2000 cm^{-1} lower in energy from the lowest ^{1}MLCT absorption maxima at room temperature. The phosphorescence maxima are observed around 960 nm for **I** and **III** and around 900 nm for **II** and **IV** and are not related to the MLCT absorption bands. It is interesting that the phosphorescence ($^3\delta\delta$* state) energies are similar between the amide and the thioamide compounds despite the differences between oxygen and sulfur.

Upon cooling in liquid nitrogen, the fluorescence bands of **I**–**IV** shift to higher energy by ~10 nm while the phosphorescence bands shift little. Both the singlet and the

DOI: 10.1021/acs.inorgchem.6b02517
Inorg. Chem. XXXX, XXX, XXX–XXX

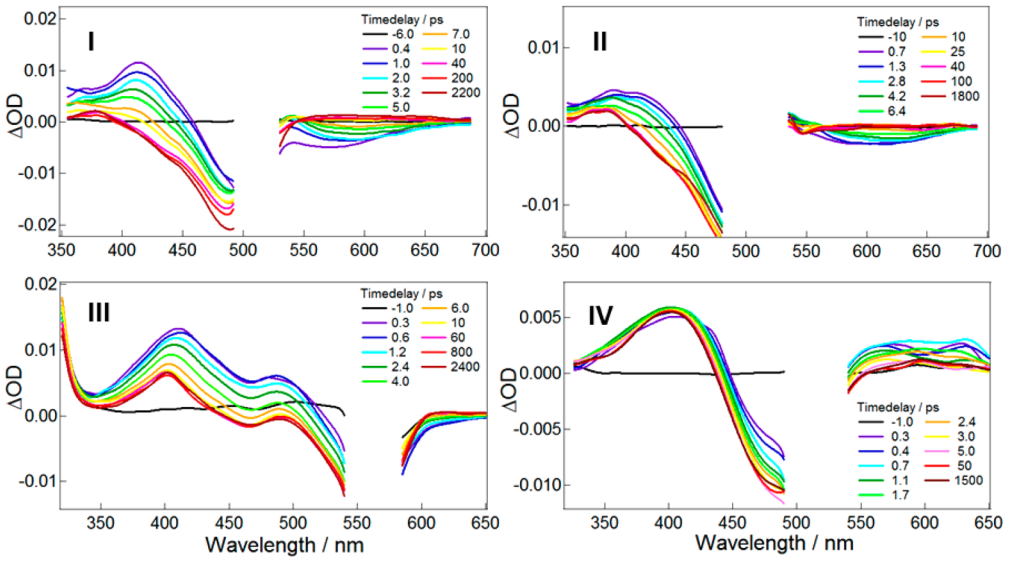

Figure 8. fs-TA spectra of **I**–**IV**, collected in THF solution at room temperature. λ_{ex} = 515 nm for **I**, **II**, and **IV**; λ_{ex} = 568 nm for **III**.

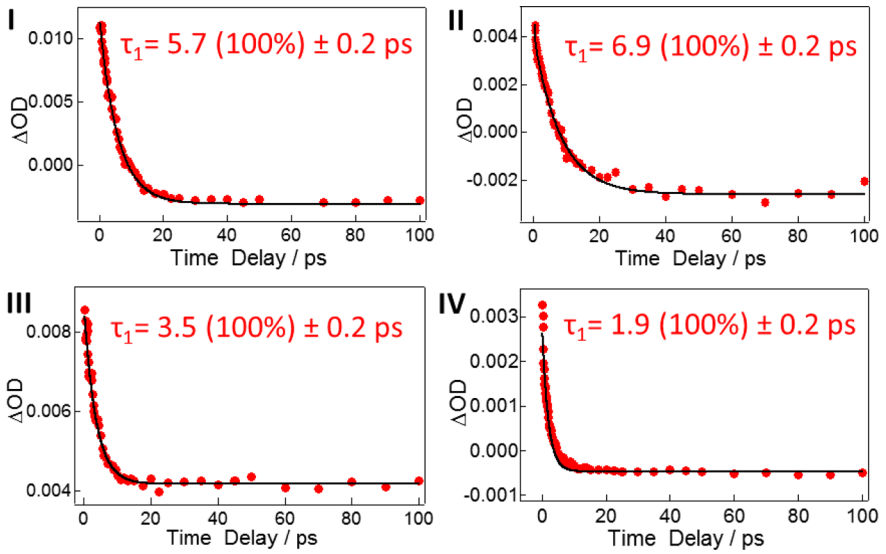

Figure 9. Kinetic traces of the early absorption feature for **I**, **II**, **III**, and **IV**. Data are taken at 420, 420, 380, and 439 nm, respectively.

triplet emission bands gain intensity where the singlet emission is more strongly affected. Vibronic progressions start to reveal themselves where shoulders of the ^{1}MLCT singlet state emission become clearer and sharp peaks in the $^3\delta\delta^*$ triplet state emission start to emerge. Vibronic coupling modes at ~300 cm^{-1} were observed in the $^3\delta\delta^*$ state emission in **I** and **III**. These vibronic features are assigned to totally symmetric vibrational modes such as Mo–Mo stretches and coordinated N–C–X stretches in the $^3\delta\delta^*$ states.[25] In compounds **II** and **IV**, the vibronic features appear to be more complex.

Transient Absorption Spectra and Excited-State Lifetimes. The excited states of **I**–**IV** were studied in THF solution by pump–probe-type transient absorption spectroscopy in both the femtosecond scale (fs-TA) and the nanosecond scale (ns-TA).

The fs-TA spectra of **I**–**IV** are shown in Figure 8 with time delays shown inset. Excitation wavelengths were set to 515 nm for **I**, **II**, and **IV** and 568 nm for **III**, all to the lower energy side of their MLCT bands. Data points around the excitation wavelength in each case were excluded due to pump laser interference. All four compounds show early features decaying on the picosecond time scale and long-lived features persisting into the nanosecond time scale, which were attributed to the lowest singlet state (S_1 states) and the lowest triplet states (T_1 states), respectively.

The short time-delay spectra of **I**–**IV** in Figure 8 (blue and purple traces) show distinctive S_1 state absorption bands. In **I** and **II**, the S_1 state absorption maxima can be determined to be between 400 and 500 nm, while in **III** and **IV**, the absorption bands are quite broad, making the specific absorption maxima difficult to identify. A strong negative band can be found at ~500 nm in **I**, **II**, and **IV**, which was attributed to ground-state bleach. In **III**, two negative bands, one at ~460 nm and one at ~560 nm, were also attributed to ground-state bleach, both consistent with the UV–vis spectra. A negative band around 580 nm in **I** and 600 nm in **II** were attributed to stimulated emission from S_1 states. The absorption bands and stimulated emission bands decay within picoseconds in a parallel manner.

The S_1 state absorption features of **I**–**IV** were all fitted with monoexponential decay functions. The lifetimes were found to

DOI: 10.1021/acs.inorgchem.6b02517
Inorg. Chem. XXXX, XXX, XXX–XXX

be 5.7, 6.9, 3.5, and 1.9 ps for **I**, **II**, **III**, and **IV**, agreeing well with the S_1 lifetimes found for previous related compounds.[14] With the spectra features and lifetimes observed, the S_1 states of **I**–**IV** are all reaffirmed as ^{1}MLCT S_1 states, Figure 9.

In the longer time-delay spectra shown in Figure 8 (red traces), the features were attributed to the T_1 state absorption and ground-state bleach. Strong absorption bands can be identified at ~350–450 nm and bleach bands at the MLCT absorption maxima of each compound. The T_1 states of **I**–**IV** at longer time scales were studied with ns-TA spectra.

In the ns-TA experiments, an excitation wavelength of 532 nm was used for all compounds. The spectra are shown in Figures S14–S17 in the Supporting Information. The T_1 state absorption bands and the ground-state bleach bands observed in ns-TA spectra were at the same positions as the fs-TA spectra. T_1 lifetimes of compounds **I**–**IV** were extracted from the absorption features and found to be 94, 84, 71, and 85 μs, respectively. These lifetimes are consistent with the $^3\delta\delta^*$ T_1 assignments, and they are longer than those found in carboxylate compounds.[14]

The S_1 and T_1 lifetimes of **I**–**IV** obtained from fs-TA and ns-TA spectra are shown in Table 4 together with results from the fs-TRIR spectra (see the Time-Resolved Infrared Spectroscopy section). The S_1 lifetimes from fs-TA and fs-TRIR experiments agree well.

Table 4. Excited-State Lifetimes of I–IV

	S_1 lifetime (ps)		T_1 lifetime (μs)
	fs-TRIR	fs-TA	ns-TA
I	5.5 ± 0.2	5.7 ± 0.2	94 ± 5
II	6.9 ± 0.2	6.9 ± 0.2	84 ± 3
III	3.5 ± 0.2	3.5 ± 0.2	71 ± 8
IV	1.6 ± 0.1	1.9 ± 0.2	83 ± 2

Time-Resolved Infrared Spectroscopy. The excited states of **I**–**IV** were also studied with fs-TRIR spectra in THF solution. Here, special interest is taken on the electron density distribution over the amide/thioamide ligands in the ^{1}MLCT S_1 states. The shift magnitudes of the IR bands on the ligands are directly correlated with the transferred electron density, and thus, they were probed carefully.

From the FT-IR spectra, compounds **I**–**IV** show three main types of IR reporter bands: (1) C≡C stretches, ν(C≡C), (2) phenyl ring stretches (in the —C≡C—Ph moieties), $\nu(C_6)_{ring}$, and (3) carboxylate, amide, and thioamide stretches, ν(O–C–O), ν(N–C–O), and ν(N–C–S). In the ground states of **I**–**IV**, ν(C≡C) appears as a weak absorption band at ~2210 cm^{-1}, $\nu(C_6)_{ring}$ as a moderate absorption band at ~1600 cm^{-1}, and ν(O–C–O), ν(N–C–O), and ν(N–C–S) as strong absorption bands in the 1200–1500 cm^{-1} region where the asymmetric modes ν_{as}(O–C–O), ν_{as}(N–C–O), and ν_{as}(N–C–S) appear at higher energy than the symmetric modes ν_s(O–C–O), ν_s(N–C–O), and ν_s(N–C–S).

For the purpose of discussing the features, the fs-TRIR spectra were divided into two regions: the 1850–2250 cm^{-1} region containing the ν(C≡C) bands and the 1350–1650 cm^{-1} region containing the $\nu(C_6)_{ring}$, ν(O–C–O), ν(N–C–O), and ν(N–C–S) bands.

fs-TRIR Spectra in the ν(C≡C) Region. fs-TRIR spectra of **I**–**IV** from 1850 to 2250 cm^{-1} are shown in Figure 10, where the inverted ground-state FT-IR spectra were also plotted together as dotted lines. At the picosecond time delays, strong ν(C≡C) bands corresponding to the ^{1}MLCT S_1 states of **I**–**IV** appear with large shifts to lower energy from their ground-state frequencies. The peak positions are marked by black arrows.

In compound **I**, two ν(C≡C) bands appeared in its ^{1}MLCT S_1 state: a weaker band at around 2152 cm^{-1} and a stronger band around 1970 cm^{-1}. Compared to the ground state, the two ν(C≡C) bands are shifted to lower energy by 53 and 235 cm^{-1}, respectively. In compound **II**, the spectra are quite similar to that of **I** where also two ν(C≡C) bands were identified, at 1970 and 2152 cm^{-1}. The shapes of the ν(C≡C) bands, however, are noticeably flatter than those of **I**.

In compound **III**, only one ν(C≡C) band was observed in the ^{1}MLCT S_1 state. The peak was found at ~2021 cm^{-1} and is noticeably sharp. This ν(C≡C) band in **III** is shifted by 189 cm^{-1} from the ground state. In compound **IV**, two ν(C≡C)

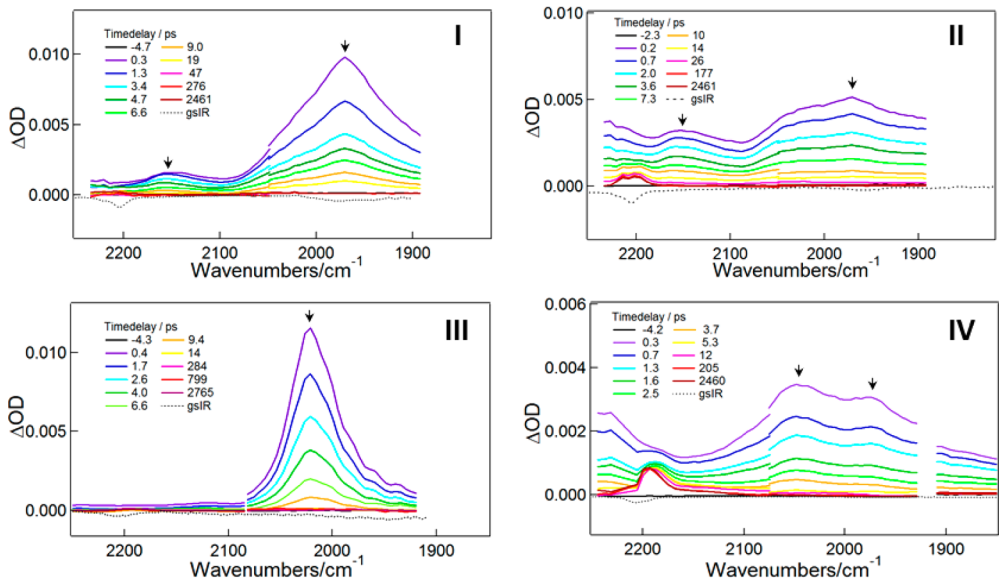

Figure 10. fs-TRIR spectra of **I**–**IV** in the region of 1850–2250 cm^{-1}. Time delays are shown as inset. Inverted ground-state IR absorption spectra (gs-IR) are also plotted as dotted lines.

DOI: 10.1021/acs.inorgchem.6b02517
Inorg. Chem. XXXX, XXX, XXX–XXX

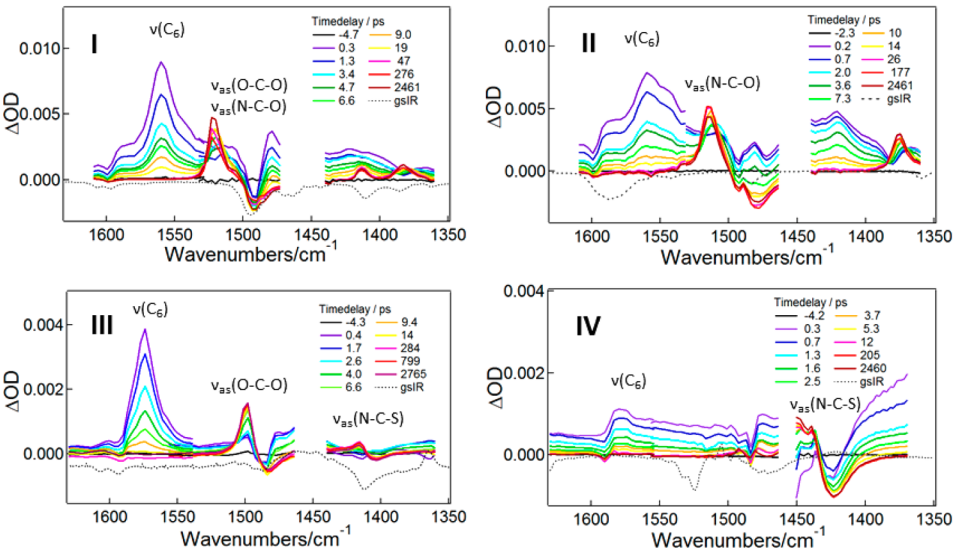

Figure 11. fs-TRIR of **I**–**IV** in the region of 1350–1650 cm^{-1} containing $\nu(C_6)_{ring}$, ν(O–C–O), ν(N–C–O), and ν(N–C–S) bands. Inverted ground-state IR absorption spectra (gs-IR) are also plotted, as dotted lines. Data points around 1450 cm^{-1} were obscured due to strong solvent absorption.

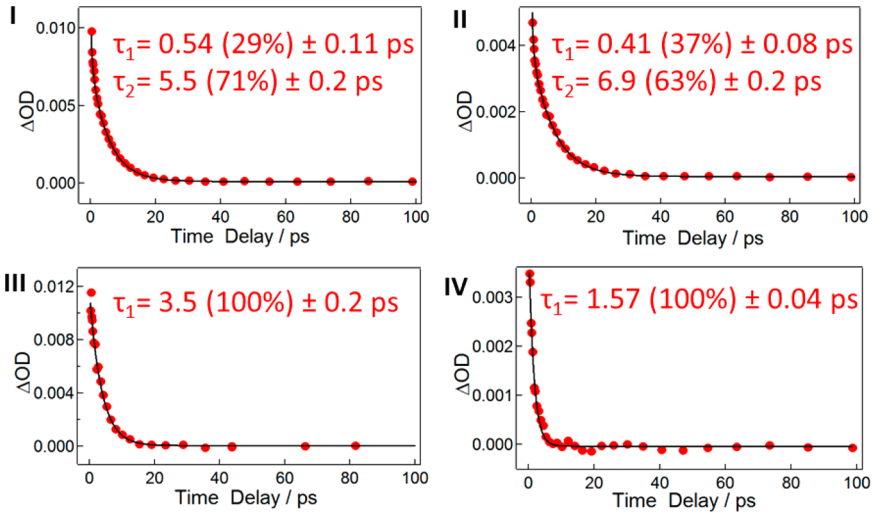

Figure 12. Kinetic traces of ν(C≡C) bands in fs-TRIR spectra of **I**, **II**, **III**, and **IV**. Data are taken at 1970, 1970, 2021, and 2048 cm^{-1}, respectively.

bands were found, at 2048 and 1974 cm^{-1}. The former is shifted by 160 cm^{-1} from the ground state, and the latter is shifted by 234 cm^{-1}. Again, the two ν(C≡C) bands in this homoleptic compound appear to be broader than that of **III**.

In a picosecond time window, the ν(C≡C) bands corresponding to the ^{1}MLCT S_1 states of **I**–**IV** decay completely and long-lived weak ν(C≡C) bands corresponding to the $^3\delta\delta^*$ T_1 states emerge at ~2200 cm^{-1}, close to their ground-state frequencies. This transformation agrees with the ^{1}MLCT S_1 to $^3\delta\delta^*$ T_1 conversion and the return of the transferred electron from the ligands to the dimetal center. It appears that the ν(C≡C) absorption bands in the $^3\delta\delta^*$ T_1 states are much weaker in comparison to those in the ^{1}MLCT S_1 states. Also, the $^3\delta\delta^*$ T_1 state ν(C≡C) absorption bands of **II** and **IV** are slightly asymmetric, probably due to ground-state bleach.

fs-TRIR Spectra in the $\nu(C_6)_{ring}$ and ν(O–C–O)/ν(N–C–O)/ν(N–C–S) Region. fs-TRIR spectra of **I**–**IV** from 1650 to 1350 cm^{-1} are shown in Figure 11. Strong features were observed corresponding to the $\nu(C_6)_{ring}$ bands in the ^{1}MLCT S_1 states and the ν(O–C–O), ν(N–C–O), and ν(N–C–S) bands in the $^3\delta\delta^*$ T_1 states.

The $\nu(C_6)_{ring}$ bands generally show similar features as ν(C≡C) bands. In the ^{1}MLCT S_1 states of **I**–**IV**, a weak bleach band at the ground-state $\nu(C_6)_{ring}$ frequency (~1595 cm^{-1}) and a strong absorption band on the lower energy side were found for $\nu(C_6)_{ring}$ modes. The shift of $\nu(C_6)_{ring}$ absorption bands is ~40 cm^{-1} in **I** and **II**, 19 cm^{-1} in **III**, and 10 cm^{-1} in **IV**. Because the phenyl ring is more remote from the bimetal center, $\nu(C_6)_{ring}$ features were not observed in the $^3\delta\delta^*$ states.

Over time, the $\nu(C_6)_{ring}$ features decay and ν(O–C–O)/ν(N–C–O)/ν(N–C–S) features grow in strength. The transition is, again, consistent with the ^{1}MLCT S_1 to $^3\delta\delta^*$ T_1 conversion. Vibrations corresponding to ν(O–C–O)/ν(N–C–O)/ν(N–C–S) in **I**–**IV** show strong bleach bands at their ground-state frequencies and strong absorption bands to higher energy. These bands shift to higher energy due to reduced back-bonding from the $Mo_2\delta$ orbital to the ligand π^* orbitals in their $^3\delta\delta^*$ T_1 states.[17]

DOI: 10.1021/acs.inorgchem.6b02517
Inorg. Chem. XXXX, XXX, XXX–XXX

Due to their closeness in energy, the ν_{as}(O−C−O) and ν_{as}(N−C−O) features overlap in the spectra of **I**. The ν_{as}(O−C−O)/ν_{as}(N−C−O) bleach band was observed at 1490 cm^{-1}, and the absorption band was observed at 1523 cm^{-1}, representing a 33 cm^{-1} shift to higher energy. The absorption bands at 1415 and 1382 cm^{-1} were assigned to ν_s(O−C−O) and ν_s(N−C−O) modes, respectively. In **II**, similar features were observed to **I**. A bleach band at 1478 cm^{-1} and an absorption band at 1516 cm^{-1} were attributed to ν_{as}(N−C−O), while an absorption band at 1375 cm^{-1} was attributed to ν_s(N−C−O). In **III**, a clear bleach band at 1484 cm^{-1} and an absorption band at 1498 cm^{-1} were assigned to ν_{as}(O−C−O). A set of weaker features at lower energy, including the bleach band at 1403 cm^{-1} and the absorption band at 1416 cm^{-1}, were assigned to ν_{as}(N−C−S). In **IV**, a broad bleach band at 1423 cm^{-1} and an absorption feature at ∼1460 cm^{-1} were assigned to ν_{as}(N−C−S).

Kinetic fitting of the fs-TRIR spectra is shown in Figure 12. Kinetic traces were taken from the ν(C≡C) absorption bands of **I**−**IV**, and the lifetimes of the ^{1}MLCT S_1 states of **I**−**IV** were extracted.

Traces of **I** and **II** were best fitted using biexponetial decay functions. The first component (<1 ps) was attributed to intramolecular cooling processes.[16] **III** and **IV** were best fitted using monoexponential decay functions. The S_1 lifetimes of **I**−**IV** were found to be 5.5, 6.9, 3.5, and 1.6 ps, respectively, in close agreement with the fs-TA results.

DISCUSSION

The ν(C≡C) shifts of compounds **I**−**IV** from fs-TRIR experiments and from DFT calculations are summarized in Table 5. As mentioned previously, we calculated the ν(C≡C) shifts in the $^3\delta\delta^*$ T_1 states (^{3}**I**′−^{3}**IV**′) and estimated the ν(C≡C) shifts in the ^{1}MLCT S_1 states of **I**−**IV** using molecular anions (**I**′$^-$−**IV**′$^-$) as mimics. The vibrational shifts predicted by the molecular anion calculations correspond to completely delocalized excited states where the transferred electron resides on the two trans ligands in **I** and **III** and on all four ligands in **II** and **IV**. Compared with experimental observations, the computational results for the $^3\delta\delta^*$ T_1 states are reasonably close, but the results from anion calculations for the ^{1}MLCT S_1 states are less accurate due to deviations from completely delocalized states.

Table 5. Shift of ν(C≡C) Bands in the ^{1}MLCT S_1 and $^3\delta\delta^*$ T_1 States of I−IV[a]

	$\Delta\nu$(C≡C) S_1 (cm^{-1})		$\Delta\nu$(C≡C) T_1 (cm^{-1})	
	experimental	computational	experimental	computational
I	−53, −235	−153	3	3
II	−53, −235	−76, −104	5	5
III	−189	−126	−17	−2
IV	−160, −234	−74, −122	−15	2

[a]Notes: Computational details can be found in the Experimental Section.

In the process of examining the computational results and the fs-TRIR spectra, it becomes clear that both the coupling of C≡C stretches and the excited-state charge distribution account for the observed ν(C≡C) bands in Mo_2 paddlewheel compounds.

To better assign the observed ν(C≡C) bands, we derived all C≡C normal modes in *trans*-$Mo_2L_2(O_2C\text{-}T^iPB)_2$ and Mo_2L_4 compounds in both the ground and the MLCT excited states using group theory. The ground-state C≡C stretch modes are displayed in Figure 13. To simplify the derivation process, C_2 and C_4 point groups were used for the ground-state molecules. These results align well with frequency analyses for **I**−**IV** in the DFT calculations.

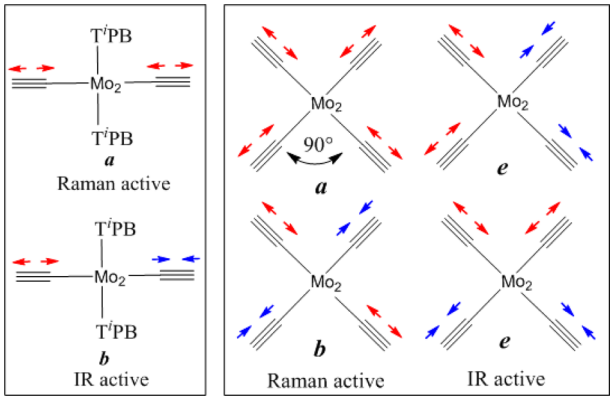

Figure 13. C≡C stretching modes in the ground state of *trans*-$Mo_2L_2(O_2C\text{-}T^iPB)_2$ and Mo_2L_4 compounds. C_2 and C_4 point groups were used for simplicity.

As shown in Figure 13, in the ground state of the *trans*-$Mo_2L_2(O_2C\text{-}T^iPB)_2$ compounds, the combination of C≡C stretches gives two ν(C≡C) normal modes: the symmetric *a* mode and the asymmetric *b* mode. The *a* mode is Raman active, and the *b* mode is IR active. With an inversion center, the Raman and IR modes here are exclusive. In the ground state of the Mo_2L_4 compounds there are four ν(C≡C) modes, namely, the *a*, *b*, and *e* modes where the symmetric *a* and *b* modes are Raman active and the degenerate *e* modes are IR active.

The MLCT-state C≡C stretching modes (with different charge distribution patterns) are displayed in Figure 14. In the MLCT excited states (including ^{1}MLCT and ^{3}MLCT states), coupling of C≡C stretches depends on molecular geometry and the molecular geometry in turn depends on charge distribution.[37,38] Thus, molecular distortions have to be considered before the derivation of coupled C≡C stretch modes. The ν(C≡C) normal modes in Figure 14 addressed all extreme localized and delocalized cases.

Figure 14A and 14B demonstrates the ν(C≡C) modes in the delocalized and the localized MLCT states of the *trans*-$Mo_2L_2(O_2C\text{-}T^iPB)_2$ compounds. In the delocalized MLCT state, the symmetry of the ground state is conserved and one Raman active mode and one IR active mode are expected. In the localized MLCT state, however, the molecule loses its symmetric structure and there would be two IR active ν(C≡C) modes. One of the IR active ν(C≡C) modes only involves the neutral ligand and would reside close to the ground-state frequency. The other mode would show a much greater shift due to the extra electron density in the singly reduced ligand.

Figure 14C−F demonstrates the ν(C≡C) modes in the MLCT states of Mo_2L_4 compounds. Overall, there are four extreme scenarios of how the transferred electron can be distributed over the four ligands. The distortions caused by the electron density distribution can be regarded as results of the excited-state Jahn−Teller effect mentioned earlier. Which exact distortion scenario is invoked depends on the electronic structure details.[37]

DOI: 10.1021/acs.inorgchem.6b02517
Inorg. Chem. XXXX, XXX, XXX−XXX

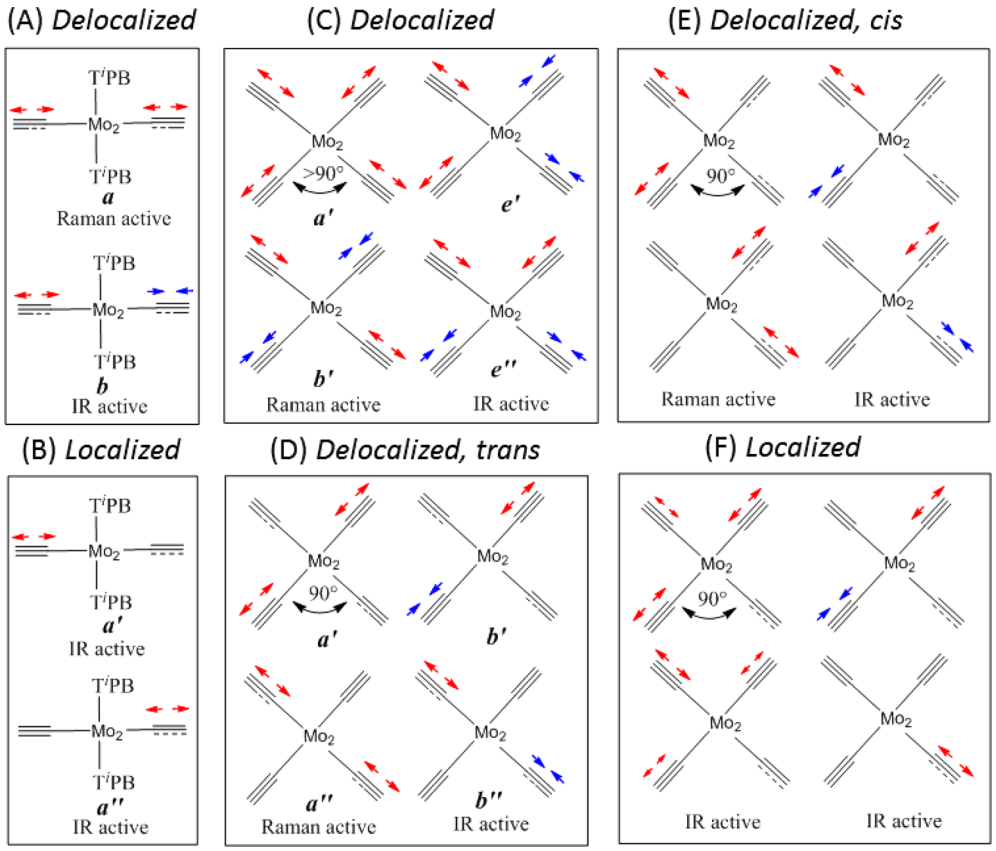

Figure 14. C≡C stretching modes in the MLCT states of *trans*-$Mo_2L_2(O_2C\text{-}T^iPB)_2$ compounds where (A) electron is delocalized and (B) electron is localized and in the MLCT states of Mo_2L_4 compounds where (C) electron is delocalized over four ligands, (D) electron is delocalized over trans ligands, (E) electron is delocalized over cis ligands, and (F) electron is localized on one ligand.

When the transferred electron is equally distributed over all four ligands, the Jahn−Teller effect would lift the degeneracy of the e orbitals which leads the dihedral angle between the cis ligands in Mo_2L_4 compounds to contract or expand. This is observed in the DFT calculation for the Mo_2L_4 anions (the optimized structures of $\mathbf{II}'^{-}$ and $\mathbf{IV}'^{-}$ are shown in Figure S9). The coupling of the C≡C stretches generates two *e*-like IR active modes, each slightly different from the *e* modes of the ground state as shown in Figure 14C. These two *e*-like modes have produced the dual ν(C≡C) bands in the anion calculations of **II** and **IV** (Table 5, Figures S11 and S13).

When the transferred electron is delocalized over only one set of trans ligands, coupling of C≡C stretches generates two IR active ν(C≡C) modes. One ν(C≡C) mode only involves the neutral ligands, and the other only involves the reduced ligands as shown in Figure 14D. In this scenario, the shift of ν(C≡C) bands observed in a Mo_2L_4 compound would be similar to a *trans*-$Mo_2L_2(O_2C\text{-}T^iPB)_2$ compound with the same acceptor ligands. When the transferred electron is delocalized over a set of cis ligands, the coupling of C≡C stretches would be in a similar way (shown in Figure 14E).

In the extreme localized case, the transferred electron resides only on one of the four ligands. As shown in Figure 14F, the coupling of C≡C stretches generates four IR active ν(C≡C) modes. Three of them involve only neutral ligands, giving overlap IR active modes close to the ground state. The remaining ν(C≡C) mode involves the singly reduced ligand and is expected to show a great shift from the ground state. The ^{1}MLCT S_1 state of compound $Mo_2[(NPh)_2CC{\equiv}CPh]_4$ studied previously was thought to be totally localized in this manner.[24]

It is clear that the group theory analyses are able to give qualitative predictions of ν(C≡C) bands of the paddlewheel compounds in the totally delocalized and totally localized MLCT states. However, the analyses provide little information on the energy and intensity of these IR active bands. The assignments of charge distribution patterns in the MLCT states of *trans*-$M_2L_2L_2$ and M_2L_4 compounds have to be based on the combination of computational and experimental results and comparison between related compounds.

In addition to these extreme cases, as we mentioned before, there are borderline cases lying between totally delocalized and localized MLCT states. To better evaluate charge distribution in the MLCT excited states, a mixed-valence classification scheme similar to the Robin−Day scheme (from class I to class III) has been used to classify them.[16,39] Following previously published works, a class I MLCT state is a charge-localized MLCT state; a class III MLCT state is a charge-delocalized MLCT state, and a class II MLCT state is an intermediate case where the barrier for electron transfer between ligands is relatively small. Since we are using infrared spectroscopy as the characterization method, any MLCT excited state where the electron transfer is much slower than the IR time scale ($\sim 10^{-12}$ s) will be perceived as class I.[40,41]

In the fs-TRIR spectra of **I**, the appearance of two ν(C≡C) bands in the ^{1}MLCT S_1 state (shifted by 53 and 235 cm^{-1}) excludes the possibility of the transferred electron being totally delocalized according to the group theory analyses. The two ν(C≡C) bands in **I** are similar to the dual ν(C≡C) bands

DOI: 10.1021/acs.inorgchem.6b02517
Inorg. Chem. XXXX, XXX, XXX−XXX

observed in compounds like $Mo_2[(NPh)_2CC{\equiv}CPh]_2(O_2C\text{-}T^iPB)_2$ (shifted by 70 and 235 cm^{-1}) and $Mo_2[(N^iPr)_2CC{\equiv}CPh]_2(O_2CMe)_2$ (shifted by 45 and 241 cm^{-1}).[16,24] Consistent with previous assignments, the appearance of two $\nu(C{\equiv}C)$ bands is attributed to two unequally reduced amide ligands in the ^{1}MLCT S_1 state of **I**, and thus, the ^{1}MLCT S_1 state of **I** is assigned as class II.

Compound **II** displayed two $\nu(C{\equiv}C)$ bands similar to **I** in the ^{1}MLCT S_1 state, and the shift magnitudes of the $\nu(C{\equiv}C)$ bands are similar as well. Thus, it is reasonable to propose that **I** and **II** have the same charge distribution pattern and the ^{1}MLCT S_1 state of **II** is also assigned as class II. With four MLCT active ligands, the transferred electron in **II** appears to be limited to one set of trans ligands, following the coupling scheme in Figure 14D. The significant breadth of the $\nu(C{\equiv}C)$ bands in **II** could be attributed to solvent interactions or exchange processes between the two sets of trans ligands.[22]

There is debate over whether the appearance of two $\nu(C{\equiv}C)$ bands (with one slightly shifted to lower energy and one greatly shifted to lower energy) fit better with the class I scenario. The class II assignment in **I** is preferred based on the lack of a second $\nu(C{\equiv}C)$ band for the ^{1}MLCT S_1 state of compound $Mo_2[(NPh)_2CC{\equiv}CPh]_4$ studied previously, which was assigned as class I.[24]

In compound **III**, the single sharp $\nu(C{\equiv}C)$ band observed in the ^{1}MLCT S_1 state suggests that **III** has a totally delocalized ^{1}MLCT S_1 state. The observed $\nu(C{\equiv}C)$ shift of 189 cm^{-1} is larger than the 124 cm^{-1} predicted by the molecular anion calculations. However, the relatively large $\nu(C{\equiv}C)$ shift could be attributed to the result of greater electron density concentration on the C≡C units in the ^{1}MLCT S_1 state of **III** relative to compounds like **I** (n.b. the $\nu(C_6)_{ring}$ bands in **III** and **IV** are shifted much less in comparison to those in **I** and **II**). The possibility that **III** could have a class I ^{1}MLCT S_1 state (if only one IR active mode appears in fs-TRIR spectra) was dismissed with the observation of the $\nu(C{\equiv}C)$ band shifted to even lower energy (234 cm^{-1}) in **IV**. The ^{1}MLCT S_1 state of **III** was then assigned as class III.

The presence of two close-lying $\nu(C{\equiv}C)$ bands in **IV** is intriguing. The number of $\nu(C{\equiv}C)$ bands fits with the charge delocalization over four ligands scenario (Figure 14C) or a partial delocalization over two trans ligands scenario (similar to Figure 14D). The observed large shift magnitudes of the $\nu(C{\equiv}C)$ bands (160 and 234 cm^{-1}) clearly exclude the former case (see computational results in Table 5). The single $\nu(C{\equiv}C)$ band observed in **III** (shifted by 189 cm^{-1}) lies between the two $\nu(C{\equiv}C)$ bands observed in **IV** (shifted by 160 and 234 cm^{-1}). Thus, the ^{1}MLCT S_1 state of **IV** was assigned as class II with reference to the class III assignment of the ^{1}MLCT S_1 state of **III**. The arrangement of the $\nu(C{\equiv}C)$ bands in **III** and **IV** raises the further suggestion of a possible coalescence process.[40]

The observation of the class II ^{1}MLCT S_1 state in **I** and the class III ^{1}MLCT S_1 state in **III** suggests that the interligand electron transfer should be much faster in **III** than in **I**. To generate different $\nu(C{\equiv}C)$ patterns in the fs-TRIR spectra, the electron transfer has to take place on the IR time scale.

The difference in interligand electron transfer can be attributed to the electronic structures of **I** and **III**, especially the HOMO and LUMO. The LUMO, in particular, represents an approximate description of the molecular orbital occupied by the transferred electron in the ^{1}MLCT S_1 state. The significant contribution from metal orbitals ($Mo_2\delta^*$) in the LUMO of **III** as shown by the DFT calculation could have promoted the electron transfer between the thioamide ligands.

Besides the differences between the amide and the thioamide ligands, the arrangements of the ligands also appear to impact on the interligand electron transfer. The amide ligands in compounds **I** and **II** adopt the same centrosymmetric arrangement, and electron transfer between the amide ligands in the ^{1}MLCT S_1 state of **I** and **II** also appears to be similar. The supporting $O_2C\text{-}T^iPB$ ligands showed limited influence on the charge distribution in **I**. The charge distribution differences in **III** and **IV** were then attributed to the distinctly arrangements of the thioamide ligands. The centrosymmetric arrangement of the thioamide ligands in **III** appears to favor faster interligand electron transfer in comparison to the mirror-symmetric arrangement in **IV**. Being of different point groups, it is hard to directly compare the electronic structures of **III** and **IV**. The LUMO of **III** does show more metal character in comparison to the LUMO+1 of **IV**, and this could be taken as evidence of different degrees of metal−ligand orbital mixing induced by ligand arrangements. The details of interligand electron transfer process require further investigation.

CONCLUSION

Consistent with our study of Mo_2 amidinate compounds,[16,24] the strong absorption of Mo_2 amide and thioamide compounds in the UV−vis region generates ^{1}MLCT S_1 excited states. The substitution of nitrogen atoms by oxygen or sulfur atoms, nevertheless, caused significant changes in the electronic structures and photophysical properties. On the basis of femtosecond time-resolved spectra, especially the observed $\nu(C{\equiv}C)$ bands in the fs-TRIR spectra, the transferred electron was found to have various distribution patterns over the amide and thioamide ligands in the ^{1}MLCT S_1 states of the paddlewheel compounds.

Using a mixed-valence classification scheme, we assigned the charge distribution in the ^{1}MLCT S_1 states of amide compounds **I** and **II** both as class II. The majority of the transferred electron density is located on one amide ligand, but some of the transferred electron density also presents on the other amide ligand (*trans* to the first). In the thioamide compounds, however, the transferred electron was found to be totally delocalized over two *trans*-thioamide ligands in the ^{1}MLCT S_1 state of **III** and unequally shared by two *trans*-thioamide ligands in the ^{1}MLCT S_1 state of **IV**. The ^{1}MLCT S_1 state of **III** is assigned as class III, and the ^{1}MLCT S_1 state of **IV** is assigned as class II.

The observed different $\nu(C{\equiv}C)$ band patterns were attributed to different rates of interligand electron transfer in the ^{1}MLCT S_1 state of these Mo_2 paddlewheel compounds. The stronger metal−ligand orbital mixing induced by sulfur atoms in thioamide compounds appears to have promoted the interligand electron transfer which yielded more delocalized ^{1}MLCT S_1 states. Ligand arrangements were also shown to influence the metal−ligand orbital mixing and interligand electron transfer in the ^{1}MLCT S_1 states.

ASSOCIATED CONTENT

Supporting Information

The Supporting Information is available free of charge on the ACS Publications website at DOI: 10.1021/acs.inorgchem.6b02517.

DOI: 10.1021/acs.inorgchem.6b02517
Inorg. Chem. XXXX, XXX, XXX−XXX

Crystal structure refinement information on **I** and **III**, NBO analysis of **I**–**IV**, nanosecond TA spectra of **I**–**IV**, NMR and MALDI-TOF mass spectra of **I**–**IV** (PDF)
Crystallographic information (CIF)
(CIF)

AUTHOR INFORMATION

Corresponding Author

*E-mail: jiang.627@osu.edu.

ORCID

Changcheng Jiang: 0000-0002-7674-6883

Present Addresses

[†]School of Chemistry, University of Nottingham, University Park, Nottingham NG7 2RD, United Kingdom.
[‡]Department of Chemistry, Northwestern University, Evanston, Illinois 60208, United States.

Notes

The authors declare no competing financial interest.

ACKNOWLEDGMENTS

We would like to thank the National Science Foundation for the funding associated with grant numbers CHE-0957191 and CHE-1266298. We are grateful to the Ohio State University Center for Chemical and Biophysical Dynamics for use of the laser systems, the Ohio Supercomputer Center for computational resources, Prof. Claudia Turro and Prof. Ewan Hamilton for useful discussion, and Prof. Prabir Dutta for use of instrumentation.

REFERENCES

(1) Grätzel, M. Photoelectrochemical Cells. *Nature* **2001**, *414*, 338–344.
(2) Chan, S. C.; Chan, M. C. W.; Wang, Y.; Che, C. M.; Cheung, K. K.; Zhu, N. Organic Light-Emitting Materials Based on Bis(arylacetylide)platinum(II) Complexes Bearing Substituted Bipyridine and Phenanthroline Ligands: Photo- and Electroluminescence from ^{3}MLCT Excited States. *Chem. - Eur. J.* **2001**, *7*, 4180–4190.
(3) Morris, A. J.; Meyer, G. J.; Fujita, E. Molecular Approaches to the Photocatalytic Reduction of Carbon Dioxide for Solar Fuels. *Acc. Chem. Res.* **2009**, *42*, 1983–1994.
(4) Sattler, W.; Ener, M. E.; Blakemore, J. D.; Rachford, A. A.; LaBeaume, P. J.; Thackeray, J. W.; Cameron, J. F.; Winkler, J. R.; Gray, H. B. Generation of Powerful Tungsten Reductants by Visible Light Excitation. *J. Am. Chem. Soc.* **2013**, *135*, 10614–10617.
(5) Demadis, K. D.; Hartshorn, C. M.; Meyer, T. J. The Localized-to-Delocalized Transition in Mixed-Valence Chemistry. *Chem. Rev.* **2001**, *101*, 2655–2686.
(6) Yeh, A. T.; Shank, C. V.; McCusker, J. K. Ultrafast Electron Localization Dynamics Following Photo-Induced Charge Transfer. *Science* **2000**, *289*, 935–938.
(7) Zhang, W.; Ji, M.; Sun, Z.; Gaffney, K. J. Dynamics of Solvent-Mediated Electron Localization in Electronically Excited Hexacyanoferrate(III). *J. Am. Chem. Soc.* **2012**, *134*, 2581–2588.
(8) Hupp, J. T.; Williams, R. D. Using Resonance Raman Spectroscopy To Examine Vibrational Barriers to Electron Transfer and Electronic Delocalization. *Acc. Chem. Res.* **2001**, *34*, 808–817.
(9) Kvapilová, H.; Sattler, W.; Sattler, A.; Sazanovich, I. V.; Clark, I. P.; Towrie, M.; Gray, H. B.; Záliš, S.; Vlček, A. Electronic Excited States of Tungsten(0) Arylisocyanides. *Inorg. Chem.* **2015**, *54*, 8518–8528.
(10) Dereka, B.; Rosspeintner, A.; Li, Z.; Liska, R.; Vauthey, E. Direct Visualization of Excited-State Symmetry Breaking Using Ultrafast Time-Resolved Infrared Spectroscopy. *J. Am. Chem. Soc.* **2016**, *138*, 4643–4649.
(11) Kiesz, M. D.; Hoekstra, R. M.; Chen, Y. T.; Telo, J. P.; Nelsen, S. F.; Zink, J. I. Coupled States in Dinitrofluorene: Relationships between Ground State and Excited State Mixed Valence. *J. Phys. Chem. A* **2014**, *118*, 11490–11498.
(12) Barlow, S.; Risko, C.; Odom, S. A.; Zheng, S.; Coropceanu, V.; Beverina, L.; Brédas, J. L.; Marder, S. R. Tuning Delocalization in the Radical Cations of 1,4-Bis[4-(diarylamino)styryl]benzenes, 2,5-Bis[4-(diarylamino)styryl]thiophenes, and 2,5-Bis[4-(diarylamino)styryl]-pyrroles through Substituent Effects. *J. Am. Chem. Soc.* **2012**, *134*, 10146–10155.
(13) Mani, T.; Grills, D. C.; Newton, M. D.; Miller, J. R. Electron Localization of Anions Probed by Nitrile Vibrations. *J. Am. Chem. Soc.* **2015**, *137*, 10979–10991.
(14) Chisholm, M. H.; Brown-Xu, S. E.; Spilker, T. F. Photophysical Studies of Metal to Ligand Charge Transfer Involving Quadruply Bonded Complexes of Molybdenum and Tungsten. *Acc. Chem. Res.* **2015**, *48*, 877–885.
(15) Alberding, B. G.; Chisholm, M. H.; Gustafson, T. L.; Liu, Y.; Reed, C. R.; Turro, C. Photophysical Studies of *trans*-Bis(phenylethynyldiisopropylamidinato)bis(acetato)dimetal Complexes Involving MM Quadruple Bonds Where M = Mo or W. *J. Phys. Chem. A* **2010**, *114*, 12675–12681.
(16) Alberding, B. G.; Chisholm, M. H.; Gallucci, J. C.; Ghosh, Y.; Gustafson, T. L. Electron Delocalization in the S_1 and T_1 Metal-to-Ligand Charge Transfer States of *trans*-Substituted Metal Quadruply Bonded Complexes. *Proc. Natl. Acad. Sci. U. S. A.* **2011**, *108*, 8152–8156.
(17) Alberding, B. G.; Chisholm, M. H.; Gustafson, T. L. Detection of the Singlet and Triplet MM $\delta\delta^*$ States in Quadruply Bonded Dimetal Tetracarboxylates (M = Mo, W) by Time-Resolved Infrared Spectroscopy. *Inorg. Chem.* **2012**, *51*, 491–498.
(18) Alberding, B. G.; Chisholm, M. H.; Chou, Y.-H.; Gallucci, J. C.; Ghosh, Y.; Gustafson, T. L.; Patmore, N. J.; Reed, C. R.; Turro, C. Quadruply Bonded Dimetal Units Supported by 2,4,6-Triisopropylbenzoates $MM(T^iPB)_4$ (MM = Mo_2, MoW, and W_2): Preparation and Photophysical Properties. *Inorg. Chem.* **2009**, *48*, 4394–4399.
(19) Alberding, B. G.; Brown-Xu, S. E.; Chisholm, M. H.; Gustafson, T. L.; Reed, C. R.; Naseri, V. Photophysical Properties of MM Quadruply Bonded Complexes (M = Mo, W) Supported by Carboxylate Ligands: Charge Delocalization and Dynamics in S_1 and T_1 States. *Dalton Trans.* **2012**, *41*, 13097–13104.
(20) Brown-Xu, S. E.; Chisholm, M. H.; Durr, C. B.; Spilker, T. F. Concerning the Ground State and S_1 and T_1 Photoexcited States of the Homoleptic Quadruply Bonded Complexes $Mo_2(O_2CC_6H_4$-*p*-X$)_4$, Where X = C≡C−H or C≡N. *J. Phys. Chem. A* **2013**, *117*, 13893–13898.
(21) Chisholm, M. H.; Lear, B. J. $M_2\delta$ to Ligand π-Conjugation: Testbeds for Current Theories of Mixed Valence in Ground and Photoexcited States of Molecular Systems. *Chem. Soc. Rev.* **2011**, *40*, 5254–5265.
(22) Stark, C. W.; Schreier, W. J.; Lucon, J.; Edwards, E.; Douglas, T.; Kohler, B. Interligand Electron Transfer in Heteroleptic Ruthenium(II) Complexes Occurs on Multiple Time Scales. *J. Phys. Chem. A* **2015**, *119*, 4813–4824.
(23) Bunting, P.; Chisholm, M. H.; Gallucci, J. C.; Lear, B. J. Extent of $M_2\delta$ to Ligand π-Conjugation in Neutral and Mixed Valence States of Bis(4-isonicotinate)-bis(2,4,6-triisopropylbenzoate) Dimetal Complexes (MM), Where M = Mo or W, and Their Adducts with Tris(pentafluorophenyl)boron. *J. Am. Chem. Soc.* **2011**, *133*, 5873–5881.
(24) Jiang, C.; Young, P. J.; Durr, C. B.; Spilker, T. F.; Chisholm, M. H. Synthesis, Structure, and Photophysical Properties of $Mo_2(NN)_4$ and $Mo_2(NN)_2(T^iPB)_2$, Where NN = *N*,*N*′-Diphenylphenylpropiolamidinate and T^iPB = 2,4,6-Triisopropylbenzoate. *Inorg. Chem.* **2016**, *55*, 5836–5844.
(25) In *Multiple Bonds between Metal Atoms*, 3rd ed.; Cotton, F. A., Murillo, C. A., Walton, R. A., Eds.; Springer Science and Business Media: New York, 2005.

DOI: 10.1021/acs.inorgchem.6b02517
Inorg. Chem. XXXX, XXX, XXX–XXX

(26) Hicks, J.; Ring, S. P.; Patmore, N. J. Tuning the Electronic Structure of Mo−Mo Quadruple Bonds by N for O for S Substitution. *Dalton Trans.* **2012**, *41*, 6641−6650.
(27) Armarego, W. L. F.; Chai, C. L. L. In *Purification of Laboratory Chemicals*, 5th ed.; Butterworth-Heinemann: Amsterdam, Boston, 2003.
(28) Frisch, M. J.; Trucks, G. W.; Schlegel, H. B.; Scuseria, G. E.; Robb, M. A.; Cheeseman, J. R.; Scalmani, G.; Barone, V.; Mennucci, B.; Petersson, G. A.; Nakatsuji, H.; Caricato, M.; Li, X.; Hratchian, H. P.; Izmaylov, A. F.; Bloino, J.; Zheng, G.; Sonnenberg, J. L.; Hada, M.; Ehara, M.; Toyota, K.; Fukuda, R.; Hasegawa, J.; Ishida, M.; Nakajima, T.; Honda, Y.; Kitao, O.; Nakai, H.; Vreven, T.; Montgomery, J. A., Jr.; Peralta, J. E.; Ogliaro, F.; Bearpark, M.; Heyd, J. J.; Brothers, E.; Kudin, K. N.; Staroverov, V. N.; Kobayashi, R.; Normand, J.; Raghavachari, K.; Rendell, A.; Burant, J. C.; Iyengar, S. S.; Tomasi, J.; Cossi, M.; Rega, N.; Millam, J. M.; Klene, M.; Knox, J. E.; Cross, J. B.; Bakken, V.; Adamo, C.; Jaramillo, J.; Gomperts, R.; Stratmann, R. E.; Yazyev, O.; Austin, A. J.; Cammi, R.; Pomelli, C.; Ochterski, J. W.; Martin, R. L.; Morokuma, K.; Zakrzewski, V. G.; Voth, G. A.; Salvador, P.; Dannenberg, J. J.; Dapprich, S.; Daniels, A. D.; Farkas, Ö.; Foresman, J. B.; Ortiz, J. V.; Cioslowski, J.; Fox, D. J. In *Gaussian 09*; Gaussian, Inc.: Wallingford, CT, 2009.
(29) Andrae, D.; Häußermann, U.; Dolg, M.; Stoll, H.; Preuß, H. Energy-Adjusted *ab initio* Pseudopotentials for the Second and Third Row Transition Elements. *Theor. Chim. Acta* **1990**, *77*, 123−141.
(30) Irikura, K. K.; Johnson, R. D.; Kacker, R. N. Uncertainties in Scaling Factors for *ab initio* Vibrational Frequencies. *J. Phys. Chem. A* **2005**, *109*, 8430−8437.
(31) Burdzinski, G.; Hackett, J. C.; Wang, J.; Gustafson, T. L.; Hadad, C. M.; Platz, M. S. Early Events in the Photochemistry of Aryl Azides from Femtosecond UV/Vis Spectroscopy and Quantum Chemical Calculations. *J. Am. Chem. Soc.* **2006**, *128*, 13402−13411.
(32) Wang, J.; Burdzinski, G.; Kubicki, J.; Platz, M. S. Ultrafast UV−Vis and IR Studies of *p*-Biphenylyl Acetyl and Carbomethoxy Carbenes. *J. Am. Chem. Soc.* **2008**, *130*, 11195−11209.
(33) Dolinar, B. S.; Berry, J. F. Electronic Tuning of Mo_2(thioamidate)$_4$ Complexes through π-System Substituents and *cis*/*trans* Isomerism. *Dalton Trans* **2014**, *43*, 6165−6176.
(34) Glendening, E. D.; Reed, A. E.; Carpenter, J. E.; Weinhold, F. *NBO*, Version 3.1.
(35) Lu, T.; Chen, F. Multiwfn: A Multifunctional Wavefunction Analyzer. *J. Comput. Chem.* **2012**, *33*, 580−592.
(36) Norman, J. G.; Kolari, H. J.; Gray, H. B.; Trogler, W. C. Electronic Structure of Dimolybdenum Tetraformate, Dimolybdenum-(4+) Ion, and Dimolybdenum. *Inorg. Chem.* **1977**, *16*, 987−993.
(37) Bersuker, I. B. *The Jahn-Teller Effect and Vibronic Interactions in Modern Chemistry*; Modern Inorganic Chemistry; Plenum Press: New York, 1984.
(38) Scattergood, P. A.; Delor, M.; Sazanovich, I. V.; Bouganov, O. V.; Tikhomirov, S. A.; Stasheuski, A. S.; Parker, A. W.; Greetham, G. M.; Towrie, M.; Davies, E. S.; et al. Electron Transfer Dynamics and Excited State Branching in a Charge-Transfer Platinum(II) Donor−bridge-Acceptor Assembly. *Dalton Trans* **2014**, *43*, 17677−17693.
(39) Plummer, E. A.; Zink, J. I. Excited-State Mixed Valence in Transition Metal Complexes. *Inorg. Chem.* **2006**, *45*, 6556−6558.
(40) Ito, T.; Hamaguchi, T.; Nagino, H.; Yamaguchi, T.; Kido, H.; Zavarine, I. S.; Richmond, T.; Washington, J.; Kubiak, C. P. Electron Transfer on the Infrared Vibrational Time Scale in the Mixed Valence State of 1,4-Pyrazine- and 4,4′-Bipyridine-Bridged Ruthenium Cluster Complexes. *J. Am. Chem. Soc.* **1999**, *121*, 4625−4632.
(41) Rocha, R. C.; Shreve, A. P. Exploring the Localized-to-Delocalized Boundary in Mixed-Valence Systems Using Infrared Spectroelectrochemistry. *Inorg. Chem.* **2004**, *43*, 2231−2233.

DOI: 10.1021/acs.inorgchem.6b02517
Inorg. Chem. XXXX, XXX, XXX−XXX